SPE-189874-MS

Benchmark Modeling of Hydraulic Fracture Interaction with Pre-Existing Fractures: Impact on Fracture Geometry, Proppant Distribution and Microseismic Response

S.C. Maxwell (Itasca-IMaGE), J. Hazzard and W. Pettitt (Itasca Consulting Group)

This paper was prepared for presentation at the SPE Hydraulic Fracturing Technology Conference held in The Woodlands, TX, USA, 23-25 January 2018.

Abstract

A modeling exercise was performed investigating hydraulic fracture interaction with pre-existing fractures, based on a benchmark modeling exercise lead by ARMA (American Rock Mechanics Association). The modeled scenarios are based on interaction with two existing faults under different geomechanical conditions. Simulations were performed with a coupled hydraulic-geomechanical-seismological, discrete-element model. The results show that the hydraulic fracture aperture is restricted at the intersection with the faults, to a degree depending on the slip induced on the fault. The aperture restriction was found to also limit the extent of the proppant distribution. In scenarios with relatively more slip, the fault activation was found to occur above and below the injection layer and resulted in some hydraulic fracture height growth relative to the depth contained fracture occurring without fault activation. As expected, the fault slip and intensity of associated microseismicity is related to the geomechanical prepotency for slip. Fractures oriented at 30° to the hydraulic fracture and maximum principal stress direction, resulted in the largest microseismic magnitude and significant hydraulic fracture restriction at the fault intersection. With increasing angle, the magnitude decreased and the hydraulic fracture had a larger half-length. Increasing the differential stress resulted in increased magnitudes and decreased fracture half-length, as did the case of a weaker fault. The study demonstrates through a numerical-physics simulation how a hydraulic fracture system behalves as it interacts with a pre-existing fracture under various geomechanical conditions.

Introduction

Hydraulic fracture treatments in unconventional reservoirs are commonly assumed to result in complex fracture networks (e.g., Maxwell et al., 2002, Mayerhofer et al., 2008), in contrast with simple hydraulic fractures that can be simulated by traditional planar fracture models (Mack and Warpinski, 2000). Interactions with reservoir heterogeneity, including bulk material properties, state of stress and pre-existing weaknesses create these complex fracture networks. Although direct observations of fracture systems have been limited, many show fracture complexity and not just a simple planar hydraulic fracture (Cipolla et al., 2008). The multitude of microseismic observations during hydraulic fracturing also suggests fracture complexity is commonplace in many unconventional reservoirs. Indeed, microseismic has prompted a paradigm shift in conceptualizing a hydraulic fracture away from a planar fracture towards a concept if a stimulated reservoir volume. Hydraulic fracture growth is ultimately controlled by the geomechanical responses of the reservoir to the injection, the impact of which is typically simplified and sometimes ignored in common planar fracture models.

Complex fracture networks can be simulated using a coupled hydraulic-geomechanical model (Damjanac and

Cundall, 2014). There are various types of models in this category, but here we focus on a 3D, discrete-element method that explicitly handles multiple pre-existing planes of weakness (i.e. fractures) in any orientation. The method computes pressure changes along the fracture system through the injection, and the associated change in mechanical response. The method is tightly coupled such that mechanical changes to the fracture aperture and stability control the hydraulic characteristics, while the pressure changes can lead to changes in the local stress field through deformable blocks between fractures and tensile or shear slip based on a characteristic constitutive parameterization of fracture failure (e.g. Mohr-Coulomb). Instantaneous slip in the model is then associated with a corresponding microseismic catalog, including time, location, moment magnitude and moment tensor (e.g. Maxwell et al., 2015). The synthetic microseismic can be used to understand the geomechanical conditions that result in various microseismic patterns (e.g. Hull et al., 2017), or to history match to field observations to calibrate the geomechanical model (e.g. Chorney et al., 2016).

Recently, the American Rock Mechanics Association's (ARMA) Hydraulic Fracturing Community proposed a benchmark 'fracture run-off' modeling exercise and openly invited various modelers to compare the output of specific models. The benchmarking defined seven different scenarios, from single fractures in different geomechanical conditions to interactions between multiple fractures. The goal of the ARMA exercise was to allow comparison on different models computed with the same parameters to demonstrate model validity and diversity to capture recognized physics. One of the benchmark scenarios (identified by ARMA as Case 5) is to model a single hydraulic fracture interaction with pre-existing fractures and is the focus of this paper.

In this paper, we describe the results of modeling the fracture interaction with pre-existing fractures as reported to ARMA. The example highlights a controlled numeric study that demonstrates how a primary hydraulic fracture interacts with pre-existing fractures in different geomechanical conditions, leveraging an ARMA benchmark test. The results provide important insights into growth and proppant distribution of complex hydraulic fracture networks, including the associated microseismic response, that can assist interpretation of microseismic images. The study also has implications to mitigating induced seismicity associated with hydraulic fracturing.

ARMA Model

The case 5 ARMA model involves a single, vertical hydraulic fracture in a multilayered formation with two pre-existing vertical fractures at different angles to the hydraulic fracture. The pre-existing vertical fractures are prescribed to be large and continuous, with each fracture located 150 feet either side of the fracture initiation 'perforation' location (as shown in Figure 1). Due to the significant dimension of the pre-existing fracture, we will refer to as a fault. Depth of the perforation is at 8000 feet. The treatment involved 20 minutes of injection at 20 bbl/min with a fluid system with density of 165 lb/ft3 and a viscosity 1 cp. 40/70 mesh sized proppant was included at a concentration of 2 ppa.

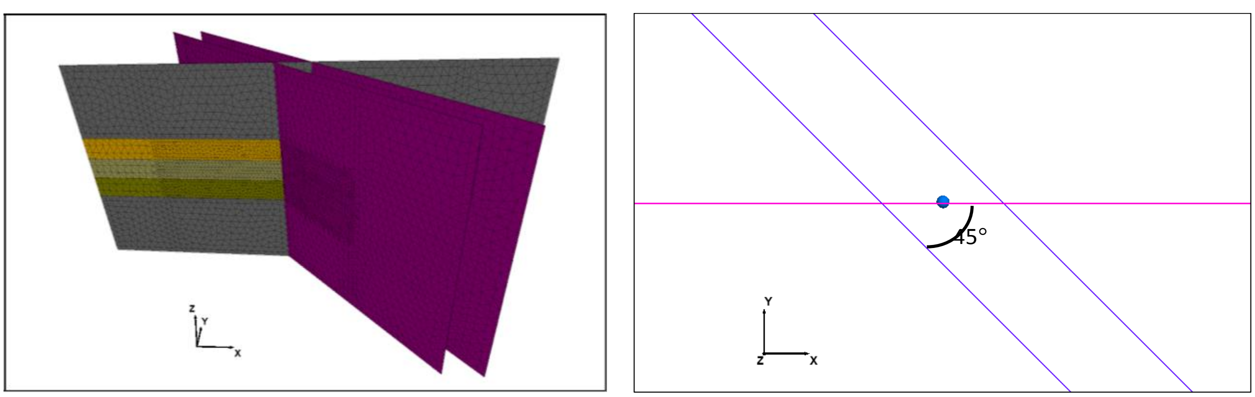

Figure 1. Perspective view (left) of the hydraulic fracture showing depth layering (light green represents injection layer) and faults (purple). Map view (right) showing the hydraulic fracture (pink) and faults (purple). Central dot shows in the fracture initiation point.

For the fractures, the base case characteristics are defined as:

- 45° angle to hydraulic fracture
- a stress contrast of 300 psi (between minimum and maximum horizontal stresses)
- coefficient of friction of 0.6

The following table describes the mechanical properties of the layers:

	Layer Top	Layer Thickness	Young's Modulus	Poisson's Ratio	KIc
	ft	ft	MMpsi		psi-in0.5
Layer 1	7700	200	3.5	0.35	500
Layer 2	7900	200	4	0.3	1000
Layer 3	8100	200	4.5	0.25	1500

	Min Horiz Stress	Max Horiz Stress	Vertical Stress	Pore Pressure
	psi	psi	psi	psi
Layer 1	5250	5550	7000	3900
Layer 2	5000	5300	7000	4000
Layer 3	5250	5550	7000	4100

Although not explicitly specified in the ARMA model, a few additional assumptions were made:

- gravity effects were not modeled to honor defined pore pressure and stress gradients
- initial fracture aperture set at 0.0004 inches
- fracture normal stiffness set at 1.67 x 10 psi/foot
- cohesion was not included
- fractures are impermeable until slip or opening occurs
- matrix leak-of options were not included
- proppant settling and bridging options were not included

Sensitivity studies were also performed to vary individual parameters relative to the base case:

- coefficient of friction of 0.3
- Intersection angle (30°, 45°, 60°, 90°)
- Stress contrast (100 psi, 300 psi, 1000 psi)

3DEC Model

The scenario was modeled using a discrete-element program (3DEC) that models assemblies of deformable blocks separated by discontinuities (Damjanac and Cundall, 2014). Movement and even complete detachment can occur between the blocks. The deformation of the blocks is calculated using the finite volume method, and the calculations are explicit, meaning that changes in stress and displacement are tracked through time enabling the simulation of highly non-linear behavior.

Fluid flow through the discontinuities is calculated assuming laminar flow through parallel plates (the rate of flow is proportional to the aperture cubed). The model exhibits full fluid-mechanical coupling such that changes in fluid pressure cause movement of the blocks, and opening and closing of faults cause pressure changes.

Base Case Model

Simulation of the base case model is shown in Figure 2. The hydraulic aperture shows a symmetric hydraulic fracture contained within the injection layer, with a small amount of opening above the layer. The aperture shows a reduction at the point of intersection with the faults. Proppant concentration was found to also be contained to the hydraulic fracture within the injection layer, mostly between the fault intersections. There was no proppant in the model located within the fault. A perspective view of a portion of the fault and hydraulic fracture shows areas of slip and the modeled pressure profile. The hydraulic fracture opens under tension (mode 1), while the fault slips under shear (mode 2). There is a larger modeled pressure drop along the fault compared to the hydraulic fracture associated with less aperture in the fault opening partially against SHmax. There is some vertical deformation of the fault outside of the injection layer, particularly above, which results in the slight upwards hydraulic fracture growth.

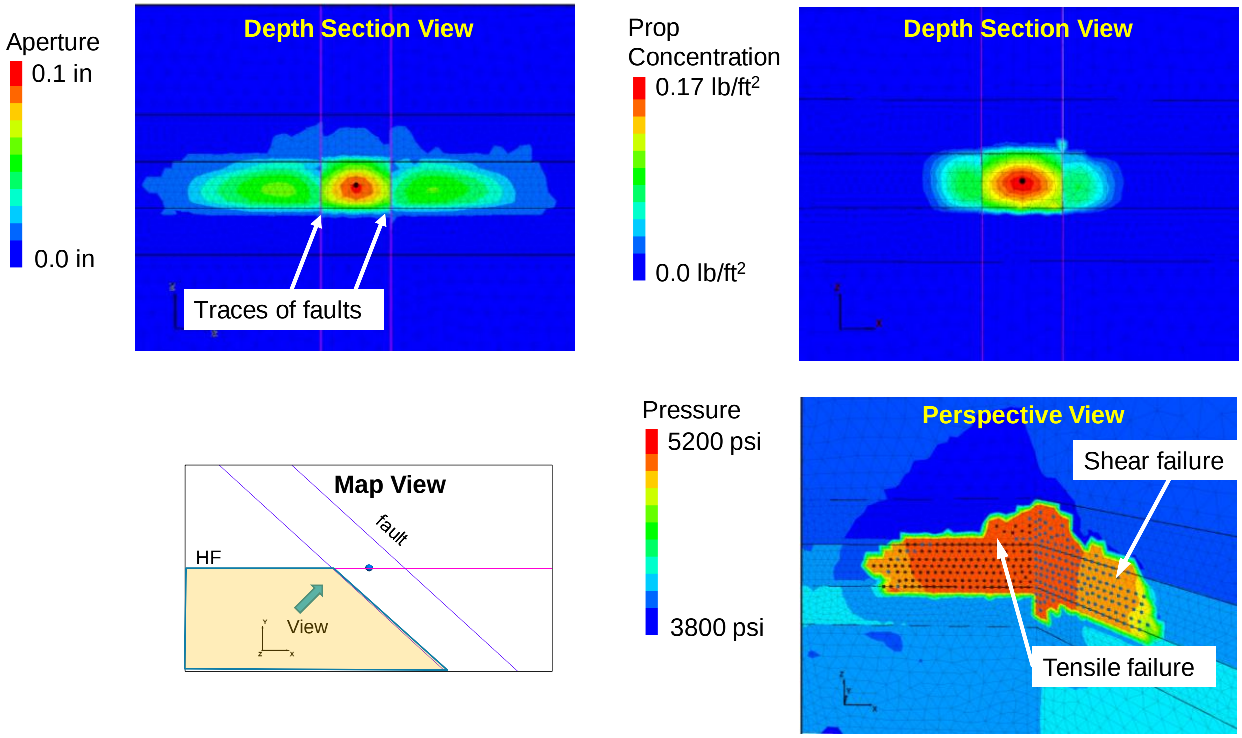

Figure 2. Depth section of the hydraulic fracture aperture (upper left) and proppant concentration (upper right) for the base-case scenario. A perspective view of a portion of the hydraulic fracture and one of the faults (lower right) with contours of pore pressure at the end of the simulation from a view point shown in the lower left. The perspective view is a cut-away as shown by the yellow region, including the left most portion of the hydraulic fracture and bottom most portion of the left fault.

Figure 3 shows the displacement field at the depth of the injection. Between the faults near the perforations, the hydraulic fracture is undergoing classic model 1 tensile opening. The fault is experiencing predominantly mode 2 shearing (so called double-couple mechanisms in the seismological community), although portions of the faults near the opening hydraulic fracture experience a more complicated, deformation mode.

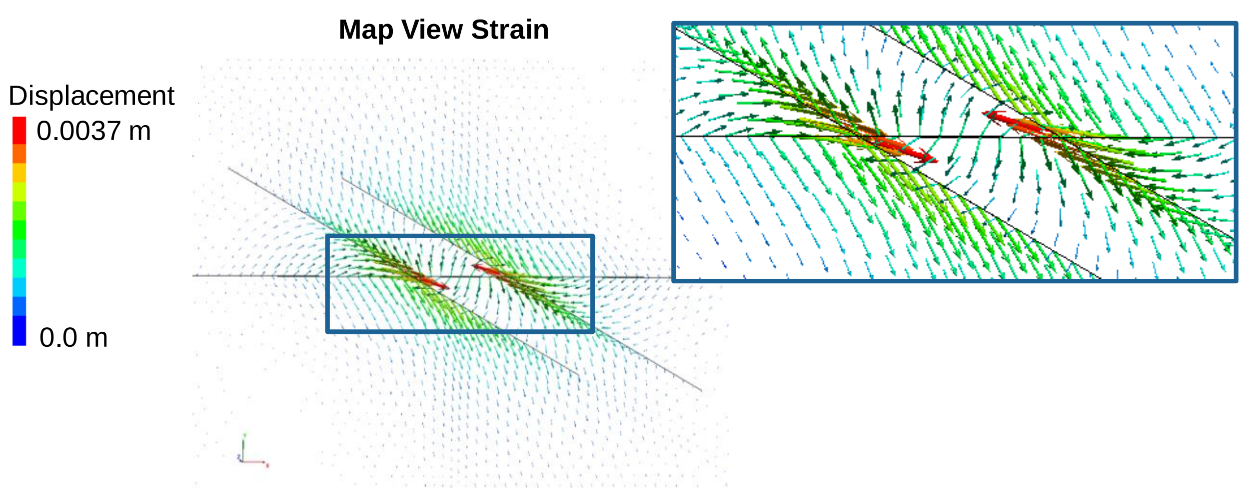

Figure 3. Map view of the geomechanical displacements computed in the model. Inset shows a zoomed in view of the region immediately around the injection point.

Angle Sensitivity

The results of modeling faults in different orientations is shown in Figure 4. At an angle of 30°, the characteristics of the fault activation observed in the base case are enhanced:

- Aperture restriction where the fault crosses the hydraulic fracture
- Muted upwards hydraulic fracture growth along the fault
- Pressure drop along the fault

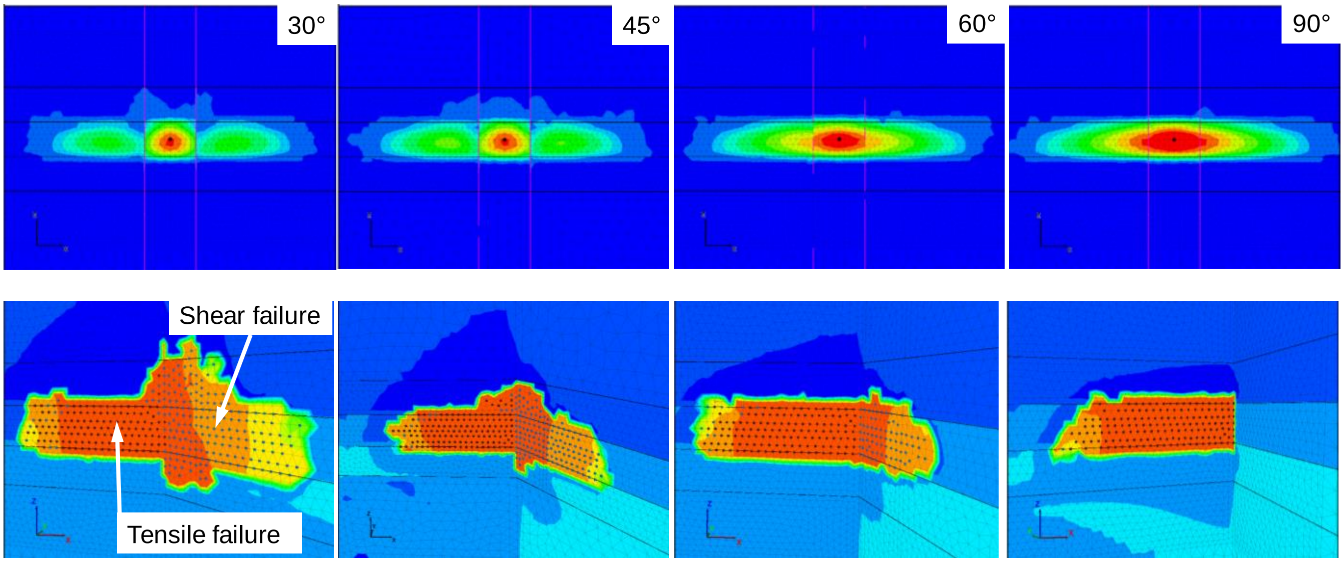

Figure 4. Progressively from left to right represent angle sensitivities at 30°, 45° (base case), 60° and 90°. Upper plots are depth view of the aperture of the hydraulic fracture, and below are perspective view of pressure contours. Views and scales are the same as Figure 2.

As the angle increases these aspects are reduced, such that by 90° the fault is not activated and the hydraulic fracture is entirely contained in the injection layer. The lack of fault activation is expected in this case, since it is aligned with a principal stress direction with no shear stress. The contained fracture is similar to a planar hydraulic fracture scenario.

Stress Sensitivity

Relative to the base case, the stress difference was reduced to 100 psi and increased to 1000 psi. At high stress difference (Figure 5), the fault activation characteristics are enhanced as described above. In this scenario, the model shows that the total hydraulic fracture length is reduced with a significant aperture restriction at the fault intersection. At lower stress difference (Figure 5), the fault activation is reduced due to less initial shear stress acting on the fault.

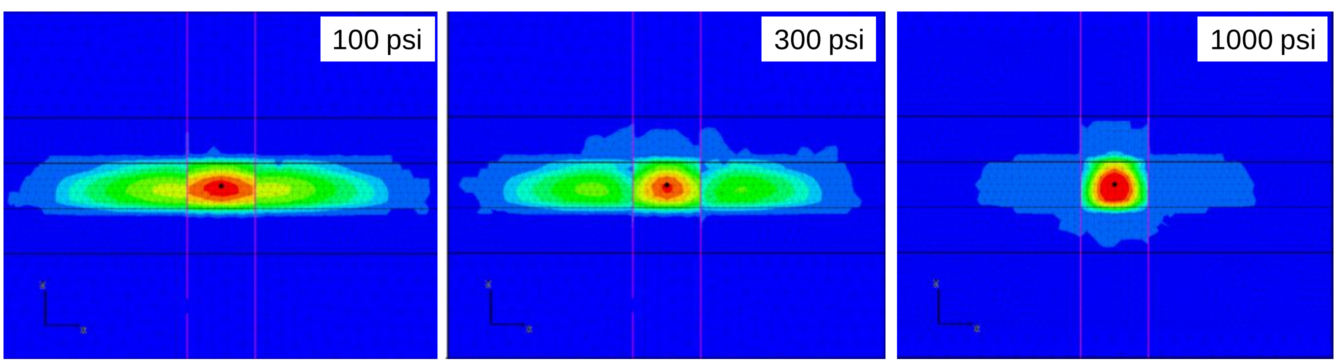

Figure 5. Aperture of the hydraulic fracture at various stress differences, scales are same as Figure 2.

Weak Fault Sensitivity

Figure 6 shows the case with a weaker fault with a coefficient of friction set at 0.3. As expected there is relatively more fault activation and the results are broadly similar to the high stress difference case, with hydraulic fracture aperture significantly reduced at the fault intersection and length reduced compared to the base case (not as restricted at the high stress difference case).

Forecasted Microseismicity

Microseismicity is simulated in the model by tracking slip on the faults. The faults are discretized into many subcontacts. The slipping and opening of all of the subcontacts are tracked over the course of the simulation. The displacements and force changes are then used to compute magnitudes for the “events”. Slipping

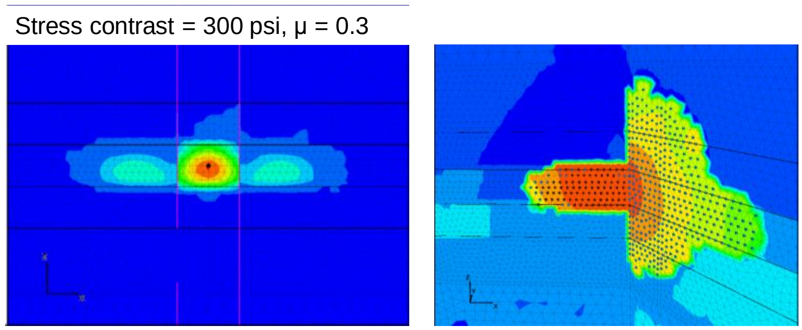

Figure 6. Hydraulic fracture aperture and perspective view of pressure contours for the weak fault model. Scales and views are the same as Figure 2.

subcontacts that are adjacent to each other and that are slipping at the same time are combined to form larger events. The centroid of the combined events is used as the microseismic location, and the seismic moment is computed from the area and displacement of slip. Moment tensor of the slip is also determined. The seismic monitoring algorithms assume a normal stress threshold of 10% of the initial value of minimum stress. This means that subcontacts that slip are not counted as seismic events if the normal stress is less than this threshold. The assumption reflects the fact that movement on joints with low normal stress or that are opening tend to be aseismic due to limited contact of the fracture faces.

The seismicity recorded over the full 20 minutes of injection for the base case model is shown in Figure 7. The fault planes are clearly delineated by seismic activity. There is a lack of seismicity on the hydraulic fracture plane, despite the fact there is opening and slip occurring here. This is because the normal confining stress along this plane is negative (meaning the plane is opening in tension due to the net pressure in the hydraulic fracture) and the slip is therefore determined to be aseismic.

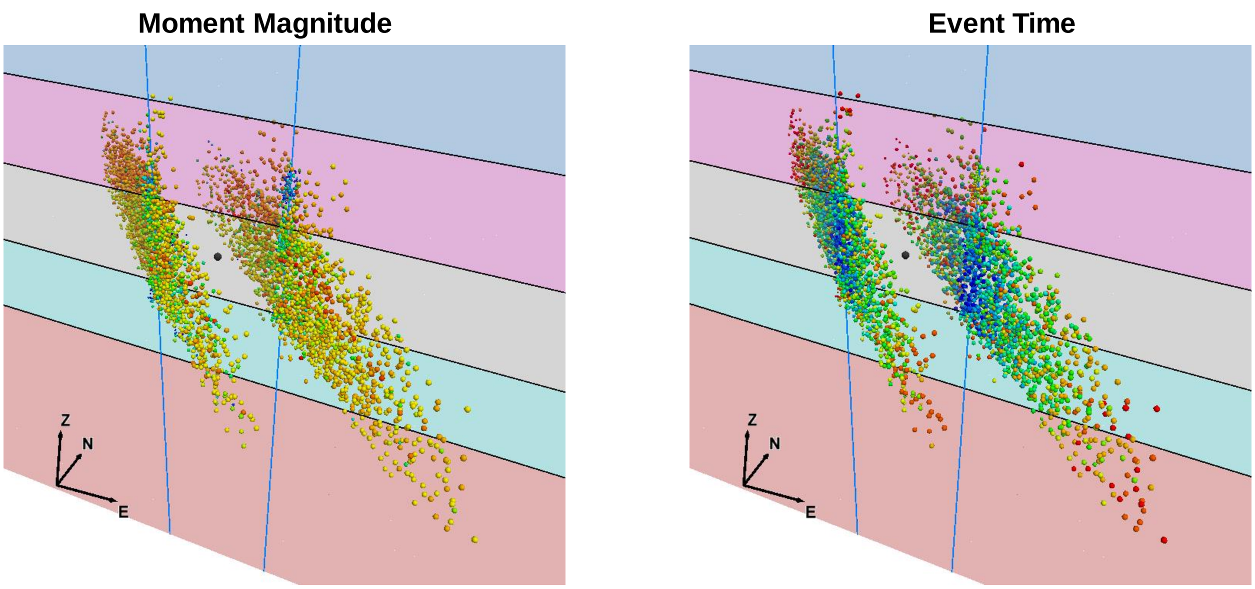

Figure 7. Perspective view of the microseismicity modeled in the base case, defining two clusters associated with each fault. On the left the microseismic are colored by moment magnitude (blue is low and red is high) and right by time (blue early and red is late).

The combination of microseismic and mechanical data in the same model enables some interesting analysis of mechanisms and the resulting seismic signature. For example, Figure 8 shows the shear displacement of the west fault with the microseismic events plotted on top. The left (north) side of the fault clearly experiences more displacement than the right (south) as previously discussed in relation to the displacement field in Figure 3. The total moment of events on the north side is correspondingly about 1.6 times the total moment of the events on the south side.

The microseismic intensity (total seismic moment and largest magnitude) computed in the models with different orientations and stress contrasts are shown in Figure 9. In terms of the different angles, the highest intensity is found for the 30° case where the preponderancy for shear slip is highest and reduces at larger angles until the

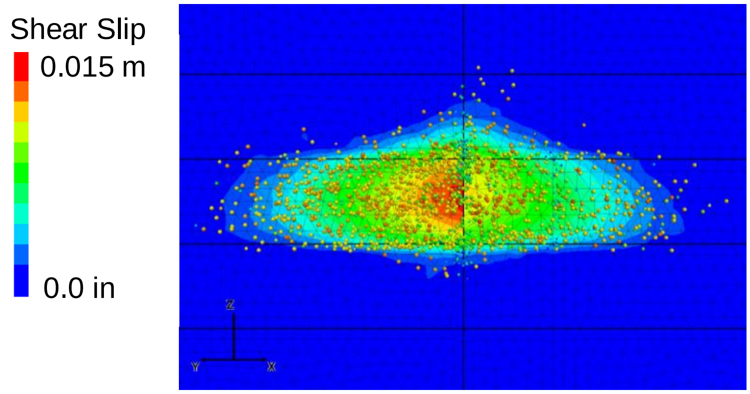

Figure 8. Depth view looking along the hydraulic fracture plane at the fault activation shown by contours of the shear slip and overlain by microseismic. Note the asymmetry of the slip about the hydraulic fracture as described around Figure 3, and less microseismicity on the right side correlating with less slip.

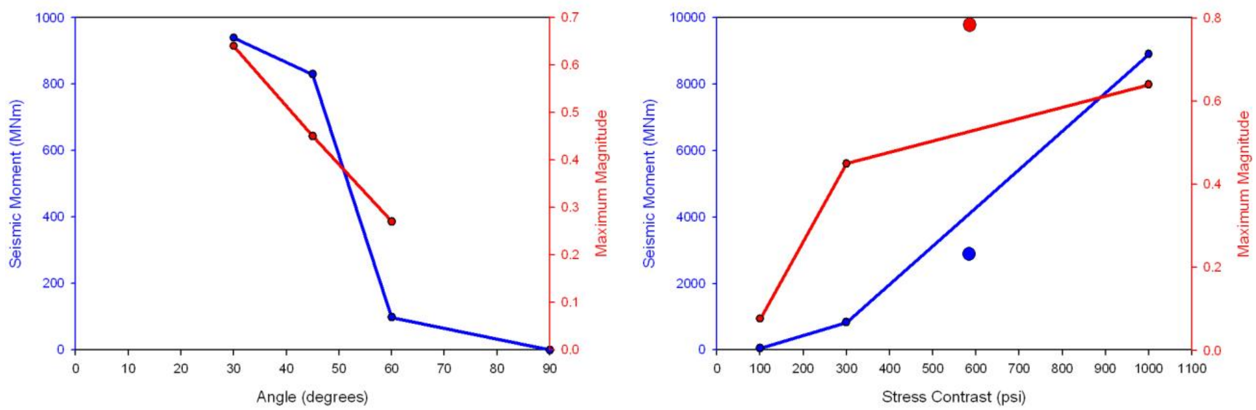

Figure 9. Total seismic moment (intensity) for all the microseismicity and largest magnitude for the angle (left) and stress difference sensitivities (right). The weak fault sensitivity are the large symbols on the right.

scenario of no microseismicity and no slip for an orthogonal fault at 90°. Stress contrast also has a significant effect on the amount and extent of seismicity, as well as the recorded magnitudes. The intensity increases as the stress contrast increases, due to increased shear stress and associated slip. The low coefficient of friction or weak fault scenario behaves similarly to the high stress contrast case.

Conclusions

To summarize, the ARMA benchmark model showed that the hydraulic fracture aperture is restricted at the intersection with the faults, to a degree depending on the slip induced on the fault. The aperture restriction was found to also limit the extent of the proppant distribution. In scenarios with relatively more slip, the fault activation was found to occur above and below the injection layer and resulted in some height growth relative to the depth contained fracture occurring without fault activation. As expected, the fault slip and intensity of associated microseismicity is related to the propensity for slip. Fractures oriented at 30° to the hydraulic fracture and maximum principal stress direction, resulted in the largest microseismic magnitude and significant hydraulic fracture restriction at the fault intersection. With increasing angle, the magnitude decreased and the hydraulic fracture had a larger half-length. Increasing the differential stress resulted in increased magnitudes and decreased fracture half-length, as did the case of a weaker fault.

References

Chorney, D., M. Smith and S.C. Maxwell, 2016, Microseismic geomechanics interpretation of a Montney hydraulic fracture, CSEG Recorder, March.

Cipolla, C. L., N. R. Warpinski, and M. J. Mayerhofer, 2008, Hydraulic fracture complexity: Diagnosis, remediation, and exploitation: Asia Pacific Oil and Gas Conference and Exhibition, SPE 115771.

Damjanac, B., and P. Cundall, 2014, Application of distinct element methods to simulation of hydraulic fracturing in naturally fractured reservoirs, in Recent Advances in Numerical Simulation of Hydraulic Fracture 2014.

Hull, R.A., S.C. Maxwell, and P.A. Leonard, 2017, Geomechanical Investigation of Microseismic Mechanisms Associated With Slip on Bed Parallel Fractures, Unconventional Resources Technology Conference, 2688667.

Mack, M., and N. Warpinski, 2000, Mechanics of hydraulic fracturing, in M. Economides and K. G. Nolte, eds., Reservoir stimulation: John Wiley and Sons.

Maxwell, S.C., M. Mack, F. Zhang, D. Chorney, S.D. Goodfellow and M. Grob, 2015, Differentiating Wet and Dry Microseismic Events Induced During Hydraulic Fracturing, Unconventional Resources Technology Conference, 2154344.

Maxwell, S. C., T. Urbancic, N. Steinsberger, and R. Zinno, 2002, Microseismic imaging of fracture complexity in the Barnett Shale: SPE 77440.

Mayerhofer, M. J., E. P. Lolon, N. R. Warpinski, C. L. Cipolla, D. Walser, and C. M. Rightmire, 2008, What is stimulated reservoir volume (SRV)?: SPE Productions and Operations, 25, 89–98, SPE 119890.